Quantum Yield in Blue-Emitting Anthracene Derivatives:

Vibronic Coupling Density

and Transition Dipole Moment Density [*]

Motoyuki Uejima[a], Tohru Sato [†a,b], Daisuke Yokoyama[c], Kazuyoshi Tanaka[a],

and Jong-Wook Park[d]

[a] Department of Molecular Engineering, Graduate School of Engineering,

Kyoto University, Nishikyo-ku, Kyoto 615-8510, Japan

[b] Unit of Elements Strategy Initiative for Catalysts & Batteries,

Kyoto University, Nishikyo-ku, Kyoto 615-8510, Japan

[c] Department of Organic Device Engineering and Research Center of Organic Electronics (ROEL),

Yamagata University, 4-3-16, Yonezawa, Yamagata 992-8510, Japan

[d] Department of Chemistry/Display Research Center,

The Catholic University of Korea, Bucheon 420-743, Republic of Korea

Submitted May 7, 2014

---

[*]Electronic supplementary information (ESI) available: (1) Duschinsky effect (2) Off-diagonal vibronic coupling density analysis; and (3) Potential energy curves in the twist angle.

[†]To whom correspondence should be addressed.

Fax: +81-75-383-2555; Tel: +81-75-383-2803; E-mail: tsato@moleng.kyoto-u.ac.jp

Abstract

Theoretical design principle for enhancement of the quantum yield of light-emitting molecules is desired. For the establishment of the principle, we focused on the S_1 states of blue-emitting anthracene derivatives: 2-methyl-9,10-di($2'$-naphthyl)anthracene (MADN), 4,9,10-bis($3',5'$-diphenylphenyl)anthracene (MAM), 9-($3',5'$-diphenylphenyl)-10-($3'',5''$- -diphenylbiphenyl-$4''$-yl) anthracene (MAT), and 9,10-bis($3''',5'''$-diphenylbiphenyl-$4'$-yl) anthracene (TAT) [Kim *et al., J. Mater. Chem.*, 2008, **18**, 3376]. The vibronic coupling constants and transition dipole moments were calculated and analyzed by using the concepts of vibronic coupling density (VCD) and transition dipole moment density (TDMD), respectively. It is found that the driving force of the internal conversions and vibrational relaxations originate mainly from the anthracenylene group. On the other hand, fluorescence enhancement results from the large torsional distortion of the side groups in the S_1 state. The torsional distortion is caused by the diagonal vibronic coupling for the lowest-frequency mode in the Franck–Condon (FC) S_1 state, which originates from a small portion of the electron density difference on the side groups. These findings lead to the following design principles for anthracene derivatives with a high quantum yield: (1) reduction in the electron density difference and overlap density between the S_0 and S_1 states in the anthracenylene group to suppress vibrational relaxation and radiationless transitions, respectively; (2) increase in the overlap density in the side group to enhance fluorescence.

2

1 Introduction

Much interest has been focused on organic light-emitting diodes (OLEDs)[1–8] because of their potential applications in full-colour large displays, lighting devices, etc. Considerable effort has been devoted to the development of red[9–12], green[9,13,14], and blue OLEDs[15–26] with desirable properties such as high luminance efficiency, long operational lifetime, pure colour coordinates, and high glass–transition temperature. However, the blue OLEDs developed so far[15–24] have shorter operational lifetime and lower luminance–efficiency than do green and red OLEDs.

Many researchers have developed blue OLEDs from anthracene derivatives[15,17,20,21,23,27]. 2-Methyl-9,10-di(2′-naphthyl)anthracene (MADN) is a well-known highly efficient blue-emitting material[15]. Recently, blue-fluorescent molecules of anthracene derivatives, 4,9,10-bis(3′,5′-diphenylphenyl)anthracene (MAM), 9-(3′,5′-diphenylphenyl)-10-(3″,5″-diphenylbiphenyl-4″-yl)anthracene (MAT), and 9,10-bis(3‴,5‴-diphenylbiphenyl-4′-yl)anthracene (TAT) (Fig. 1), have been reported to show higher quantum yields than does MADN[28].

These molecules were designed on the basis of the concept of a core moiety and a side moiety. Anthracene was selected as the core moiety, and bulky groups were introduced as the side moieties in order to prevent extensively strong π–π^* stacking interactions and to facilitate the formation of amorphous films.

The photoluminescence (PL) quantum yields of MAM, MAT, and TAT relative to MADN in solutions were measured[28]: MADN (1.00) < MAM (1.22) < MAT (1.25) < TAT (1.39). Recently, the absolute PL quantum yields of vacuum-deposited neat films of the four materials were also measured: the values for MADN, MAM, MAT, and TAT were 0.33, 0.39, 0.45, and 0.61, respectively[29].

When a molecule in the ground S_0 state absorbs a photon, there occurs a vertical excitation to a Franck–Condon (FC) state. Then, the excited molecule in the FC state undergoes structural deformation, so-called vibrational relaxation. After the vibrational relaxation, the excited

state reaches an adiabatic (AD) state. The stabilization energy, or reorganization energy due to the vibrational relaxation is the origin of the Stokes shift. The relaxation process is usually so rapid that the steady-state radiative transition comes from the AD state. There also occur radiationless transitions: internal conversion and intersystem crossing. Quantum yield depends on the competition between radiative and radiationless transitions. The vibronic couplings play an important role in the vibrational relaxation and internal conversion.

The vibronic coupling (electron–phonon coupling) is an interaction between an electron and a nuclear vibration. If the vibronic couplings are large in electron-transporting materials, the energy dissipation should be large because the hopping electron couples strongly with intramolecular vibrations[30]. The electronic part of the vibronic couplings can be represented by the electronic bases: the diagonal and off-diagonal matrix elements of the vibronic couplings are defined as the electronic parts of the diagonal and off-diagonal vibronic couplings, respectively. For a carrier-transporting molecule, the energy dissipation is ascribed to the diagonal vibronic couplings in its ionization. On the other hand, for a fluorescent molecule, the diagonal vibronic couplings give rise to the vibrational relaxation and the off-diagonal vibronic couplings drive the internal conversion. The diagonal vibronic coupling corresponds to a force with respect to a vibrational mode, and the off-diagonal couplings is an important factor of a transition probability between different electronic states[31–34]. Small diagonal vibronic coupling constants (VCCs) give rise to small vibrational relaxation, or small energy dissipation. In addition, small diagonal VCCs suppress the internal conversion, as described in Section 2.3. The small off-diagonal VCCs also contribute to a small transition rate of the internal conversion.

Therefore, small diagonal and off-diagonal VCCs are preferred for a high fluorescence quantum yield. On the other hand, the fluorescence quantum yield is increased by a large transition dipole moment. Suppression of off-diagonal VCCs and enhancement of the transition dipole moment would lead to a high quantum yield.

Vibronic coupling density (VCD) gives a local picture of a vibronic coupling[35–37]. We have

4

succeeded in controlling the vibronic couplings for carrier-transport materials on the basis of the VCD concept. We have theoretically proposed hexaaza[1_6]parabiphenylophane (HAPBP) as a hole-transport molecule with small energy dissipation, or low power loss[38] and designed hexaboracyclophane (HBCP) as an electron-transporting molecule.[39] We also analyzed the vibronic couplings in the excited state of anthracene derivatives on the basis of the VCD concept.[40] For highly efficient fluorescent materials, energy dissipation, originating from electron–phonon coupling should be reduced, and therefore reduction of VCCs is crucial. Analysis of the VCD provides an insight into the appropriate means of reducing VCCs.

Transition dipole moment density (TDMD) is a density form of the transition dipole moment[40]. The TDMD concept is similar to the VCD concept. Using the TDMD concept,[40] we have revealed why chlorinated anthracenes have large transition dipole moments. The combination of VCD and TDMD analyses enables us to control radiative and radiationless processes in a molecule.[41]

In terms of VCD, we analyze the diagonal VCCs for the excited states in blue-emitting anthracene molecules and the off-diagonal VCCs between the excited and ground states. We also analyze the transition dipole moments for the molecules in terms of the TDMD. Our final goal is to establish a principle for designing fluorescent molecules with high efficiency via the VCD and TDMD analyses of MADN, MAM, MAT, and TAT.

In Section 2, we summarize the definitions of VCC, VCD, TDMD, and related concepts. We found that the Duschinsky effect is negligible, as shown in Section S1 of the Electronic Supplementary Information (ESI). We describe the computational details in Section 3. In Section 4.1, we show the calculated transition energies and oscillator strengths for the four molecules in the FC S_1 state and the AD S_1 state. In Sections 4.2 and 4.5, we discuss the diagonal VCCs for the four molecules in the FC S_1 state and the off-diagonal VCCs between the S_1 and S_0 states, respectively. In Section 4.3, we describe the diagonal VCDs in the FC S_1 state. The off-diagonal VCDs between the S_1 and S_0 states are discussed in Section S2 of the ESI. The

5

lowest-frequency modes play a crucial role in the enhancement of radiative transitions. In Section 4.4, we present the analysis of the VCD for the lowest-frequency mode in the FC S_1 state of TAT. In Section 4.6, we discuss the difference in the transition dipole moments among the four molecules in terms of the TDMDs between the S_1 and S_0 states. We present the concluding remarks in Section 5.

2   Theory

2.1   Vibronic Coupling Constant

A molecule composed of M atoms and N electrons in the ground state is assumed to be in an equilibrium nuclear configuration $\mathbf{R_0}$. We have a set of electronic eigenfunctions $\{\Psi_n(\mathbf{r};\mathbf{R}_0)\}$ for the molecular Hamiltonian $\hat{H}(\mathbf{r},\mathbf{R})$, where $\mathbf{R} = (\mathbf{R}_1,\cdots,\mathbf{R}_A,\cdots\mathbf{R}_M)$ denotes a set of nuclear coordinates, and $\mathbf{r} = (\mathbf{r}_1,\cdots,\mathbf{r}_i,\cdots\mathbf{r}_N)$ denotes a set of electron coordinates. The matrix representation of the vibronic coupling for mode α is defined by

$$V_{mn,\alpha} = \left\langle \Psi_m(\mathbf{r},\mathbf{R}_0) \left| \left(\frac{\partial \hat{H}(\mathbf{r},\mathbf{R})}{\partial Q_\alpha} \right)_{\mathbf{R}_0} \right| \Psi_n(\mathbf{r},\mathbf{R}_0) \right\rangle, \tag{1}$$

where Q_α indicates the normal coordinate for the mode α.

The diagonal VCCs are defined as the diagonal elements of the vibronic couplings with $n = m$. They are used to calculate the reorganization energy in the FC state. For simplicity, we omit n for the diagonal VCC as follows:

$$V_{n,\alpha} = V_{nn,\alpha}. \tag{2}$$

The off-diagonal VCCs are defined as the off-diagonal elements of the vibronic couplings with $n \neq m$. A rate constant of the internal conversion is proportional to the product of the transition probability between initial and final vibronic states and the density of states of the final vibronic states, as described in Section 2.3.

6

The off-diagonal vibronic coupling is an important factor of the transition probability between vibronic states with different electronic states S_m and S_n.[31] Recently, for example, the rate constants of the internal conversions for ethylene and azulene have been calculated using the off-diagonal vibronic coupling constants.[32–34] If the off-diagonal VCC is reduced, the transition probability is decreased. Therefore, the internal conversion is suppressed and enhance the fluorescence quantum yield.

2.2 Vibronic Hamiltonian

The vibronic Hamiltonian in the FC S_n state within the crude adiabatic (CA) approximation[42] including the harmonic potential is given by

$$H_n^{\text{vibro}} = E_n + \sum_\alpha \left[-\frac{\hbar^2}{2} \left(\frac{\partial^2}{\partial Q_\alpha^2} \right) - V_{n,\alpha} Q_\alpha + \frac{1}{2} \omega_{n,\alpha}^2 Q_\alpha^2 \right], \tag{3}$$

where the directions of the normal modes are taken so that the first-order coefficients in Q_α are negative. Thus, $V_{n,\alpha}$ is positive. $\omega_{n,\alpha}$ denotes the frequency for mode α. Then, the adiabatic potential is written as

$$U_n(\mathbf{R}) = E_n + \sum_\alpha \left\{ -V_{n,\alpha} Q_\alpha + \frac{1}{2} \omega_{n,\alpha}^2 Q_\alpha^2 \right\} \tag{4}$$

$$= E_n + \sum_\alpha \left\{ \frac{1}{2} \omega_{n,\alpha}^2 \left(Q_\alpha - \frac{V_{n,\alpha}}{\omega_{n,\alpha}^2} \right)^2 - \frac{V_{n,\alpha}^2}{2 \omega_{n,\alpha}^2} \right\}. \tag{5}$$

The reorganization energy for mode α is defined as

$$\lambda_{n,\alpha} = \frac{V_{n,\alpha}^2}{2 \omega_{n,\alpha}^2}. \tag{6}$$

The total reorganization energy summed over all the active modes is given by

$$\Delta E_n^{\text{CA}} = \sum_\alpha \lambda_{n,\alpha} = \sum_\alpha \frac{V_{n,\alpha}^2}{2 \omega_{n,\alpha}^2}. \tag{7}$$

Within the Born–Oppenheimer (BO) approximation, the adiabatic potential is written as

$$E_n^{\text{BO}}(\mathbf{R}) = \langle \Psi_n(\mathbf{r}, \mathbf{R}) | \hat{H}_e(\mathbf{r}, \mathbf{R}) | \Psi_n(\mathbf{r}, \mathbf{R}) \rangle, \tag{8}$$

where $\hat{H}_e$ is electronic Hamiltonian including the nuclear–nuclear potential. Note that the BO bases $\{\Psi_n(\mathbf{r}, \mathbf{R})\}$ depend on the nuclear coordinates, while the CA bases $\{\Psi_n(\mathbf{r}, \mathbf{R}_0)\}$ are independent. Since the electronic wavefunction depends on the nuclear coordinates, calculations for various nuclear configurations $\mathbf{R}$ are required to obtain the BO potential. The reorganization energy within the BO approximation is given by

$$\Delta E_n^{\mathrm{BO}} = E_n(\mathbf{R}_n) - E_n(\mathbf{R}_0), \tag{9}$$

where $\mathbf{R}_n$ denotes the equilibrium nuclear configuration in the S_n state. Thereby, ΔE_n^{BO} can be estimated after the search for the potential minimum of the adiabatic potential surface.

Upon the vibrational relaxation, the non-linear couplings are taken into consideration about ΔE_n^{BO}. In other words, ΔE_n^{BO} incorporates the non-linear couplings and Duschinsky effect. This is because the molecules undergo the vibrational relaxations following the adiabatic potential surfaces within the BO approximation. On the other hand, ΔE_n^{CA} can be calculated from the diagonal VCCs and their frequencies using Eq. (7), that is the linear approximation. The low-frequency modes sometimes overestimate ΔE_n^{CA} within the CA approximation, because the frequency is small and the linear approximation is imposed, following Eq. (7). The validity of the CA approximation for the present systems can be examined by the following condition: $\Delta E_n^{\mathrm{BO}} \approx \Delta E_n^{\mathrm{CA}}$.

In the present study, we use $\omega_{0,\alpha}$ for the excited states, assuming that the curvatures of the adiabatic potential in the first excited state are almost the same as those in the ground state (see Section S1 in the ESI). The reorganization energy for the FC S_1 state ΔE_1^{CA} is abbreviated as ΔE or ΔE_{CA} if the explicit description of the CA approximation is needed.

2.3 Rate constant of internal conversion

Here we consider a photoexcited molecule which undergoes the internal conversion from the S_m state to the S_n state. Within the CA approximation, the initial and final states are described

8

by vibronic states $|\Phi_{mi}\rangle = |\Psi_m\rangle|\chi_{mi}\rangle$ and $|\Phi_{nj}\rangle = |\Psi_n\rangle|\chi_{nj}\rangle$, respectively, where $|\chi_{mi}\rangle$ and $|\chi_{nj}\rangle$ denote initial and final vibrational states, respectively. The rate of the internal conversion is then given by[34,43]

$$k_{m\to n}^{\text{IC}}(T) = \frac{2\pi}{\hbar} \sum_{ij} P_{mi}(T) \delta(E_n - E_m - \hbar\omega_{ij}) \left| \langle\Phi_{nj}|\hat{H}'|\Phi_{mi}\rangle \right|^2, \tag{10}$$

where $P_{mi}(T)$ describes the Boltzmann distribution of the initial vibronic states, and ω_{ij} indicates the angular frequency for a phonon. The matrix elements of the interaction Hamiltonian is given by

$$\langle\Phi_{nj}|\hat{H}'|\Phi_{mi}\rangle = \sum_{\alpha} \left\langle \Psi_n(\mathbf{r},\mathbf{R}_0) \left| \left(\frac{\partial\hat{H}(\mathbf{r},\mathbf{R})}{\partial Q_\alpha}\right)_{\mathbf{R}_0} \right| \Psi_m(\mathbf{r},\mathbf{R}_0) \right\rangle \langle\chi_{nj}|Q_\alpha|\chi_{mi}\rangle. \tag{11}$$

The rate constant of internal conversion then becomes

$$k_{m\to n}^{\text{IC}}(T) = \frac{2\pi}{\hbar} \sum_{ij} P_{mi}(T) \sum_{\alpha\beta} V_{nm,\alpha} V_{mn,\beta} \langle\chi_{nj}|Q_\alpha|\chi_{mi}\rangle\langle\chi_{mi}|Q_\beta|\chi_{nj}\rangle \delta(E_n - E_m - \hbar\omega_{ij}). \tag{12}$$

Eq. (12) is the rate constant of internal conversion within the CA approximation, indicating a rapid internal conversion occurs when off-diagonal VCCs are large. The diagonal VCCs are also the key factor to determine the rate constant because the factor $\langle\chi_{nj}|Q_\alpha|\chi_{mi}\rangle$ depends on the diagonal VCCs.

We consider the case where a vibrational mode in the S_m state is expressed in terms of those in the S_n state, meaning that the Duschinsky effect is ignored. The matrix element for vibrational states in Eq. (12) is given by

$$\langle\chi_{nj}|Q_\alpha|\chi_{mi}\rangle = \langle n'_\alpha|Q_\alpha|n_\alpha\rangle \prod_{\beta\neq\alpha} \langle n'_\beta|n_\beta\rangle, \tag{13}$$

where n_α and n'_α indicate the numbers of phonons for mode α of the initial and final states. Using the dimensionless VCC g_α, the FC overlap integral is expressed as[44]

$$\langle n'_\alpha|n_\alpha\rangle = \sqrt{\frac{n_\alpha! n'_\alpha!}{2^{n_\alpha + n'_\alpha}}} e^{-\frac{1}{4}g_\alpha^2} \sum_{l=0}^{\min[n_\alpha, n'_\alpha]} (-1)^{n'_\alpha - l} 2^l \frac{g_\alpha^{n_\alpha + n'_\alpha - 2l}}{l!(n_\alpha - l)!(n'_\alpha - l)!}, \tag{14}$$

9

where g_α is defined by[37]

$$g_\alpha = \frac{V_{n,\alpha}}{\sqrt{\hbar \omega_{n,\alpha}^3}}.$$ (15)

Therefore, the nuclear moment is given by

$$\langle n'_\alpha | Q_\alpha | n_\alpha \rangle = \sqrt{\frac{\hbar}{2\omega_\alpha}} \left(\sqrt{n_\alpha + 1} \langle n'_\alpha | n_\alpha + 1 \rangle + \sqrt{n_\alpha} \langle n'_\alpha | n_\alpha - 1 \rangle \right).$$ (16)

Accordingly, the nuclear moment is transformed into the FC overlap integrals. Thus, the IC rate constant strongly depends on the diagonal VCCs.

To understand the dependence of the rate constant of internal conversion on the VCCs, we consider only a single mode, and we do not consider temperature hereafter. Because the actual molecule interacts with the surroundings, the broadening of the density of states occurs. When the Gaussian broadening is assumed, the rate constant of the internal conversion is written as

$$k_{m \to n}^{IC} = \frac{2\pi}{\hbar} |V_{nm,\alpha}|^2 \left| \langle \chi_{nj} | Q_\alpha | \chi_{mi} \rangle \right|^2 \frac{1}{\sqrt{2\pi}\sigma} \exp\left(\frac{(E_n - E_m - \hbar\omega_{ij})^2}{2\sigma^2} \right),$$ (17)

where σ denotes the linewidth. The dependence of the rate constant on the VCC for the single mode α is shown in Figure 2. The frequency of 1400 cm^{-1} (Fig. 2(a)) and that of 1600 cm^{-1} (Fig. 2(b)) are given with the off-diagonal VCC $V_{mn,\alpha} = 3 \times 10^{-4}$ a.u. and with $\sigma = 300$ cm^{-1}. Note that the dots in Figure 2 show the point with $E_n - E_m = \hbar\omega_{ij}$. As shown in Figure 2, small diagonal VCCs give rise to small rate constant of internal conversion. The fluorescence quantum yield Φ_F is given by the rate constants of fluorescence k^F (formulated in Section 2.5) and internal conversion k^{IC}:

$$\Phi_F(T) = \frac{k^F(T)}{k^{IC}(T) + k^F(T)}.$$ (18)

Therefore, reducing the diagonal and off-diagonal VCCs leads to enhance the quantum yield.

2.4 Vibronic Coupling Density

The nuclear-electronic potential of molecule U_{en} is represented as the sum of the attracting potentials $u(\mathbf{r}_i)$ for electron i:

$$U_{en} = \sum_i u(\mathbf{r}_i) = \sum_A \sum_i -\frac{Z_A e^2}{|\mathbf{r}_i - \mathbf{R}_A|}, \tag{19}$$

where Z_A denotes the charge of nucleus A. The attracting potential acting on a single electron u is expressed as

$$u(\mathbf{x}) = \sum_A -\frac{Z_A e^2}{|\mathbf{x} - \mathbf{R}_A|}, \tag{20}$$

where $\mathbf{x} = (x, y, z)$. The derivative of potential $u(\mathbf{x})$ with respect to Q_α is given by

$$v_\alpha(\mathbf{x}) = \left(\frac{\partial u(\mathbf{x})}{\partial Q_\alpha}\right)_{\mathbf{R}_0}. \tag{21}$$

The diagonal VCD[35–37] $\eta_{n,\alpha}(\mathbf{x})$ in the FC S_n state is defined by[40]

$$\eta_{n,\alpha}(\mathbf{x}) = \Delta\rho_n(\mathbf{x})v_\alpha(\mathbf{x}), \tag{22}$$

where $\Delta\rho_n$ is the difference between the electron densities in the S_n state ρ_n and the ground state ρ_0:

$$\Delta\rho_n(\mathbf{x}) = \rho_n(\mathbf{x}) - \rho_0(\mathbf{x}). \tag{23}$$

The integral of $\eta_{n,\alpha}$ yields $V_{n,\alpha}$:

$$V_{n,\alpha} = \int \Delta\rho_n(\mathbf{x})v_\alpha(\mathbf{x})d^3\mathbf{x} = \int \eta_{n,\alpha}(\mathbf{x})d^3\mathbf{x} \tag{24}$$

The VCD enables us to discuss the VCC in terms of the electronic and vibrational structures. The delocalized $\Delta\rho$ gives rise to small VCCs.[45] When $\Delta\rho$ is symmetrically distributed around atoms, the VCC is small, even if $\Delta\rho$ is localized. This is because the positive η_α and negative η_α are cancelled in the spatial integration of η_α.[36] Thus, we can reduce the VCC by using the VCD concept. The off-diagonal VCD $\eta_{mn,\alpha}(\mathbf{x})$ between the S_m and S_n states is defined by[40]

$$\eta_{mn,\alpha}(\mathbf{x}) = \rho_{mn}(\mathbf{x})v_\alpha(\mathbf{x}), \tag{25}$$

11

where ρ_{mn} is the overlap density (transition density) between the S_m and S_n states. The integral of $\eta_{mn,\alpha}$ yields $V_{mn,\alpha}$:

$$V_{mn,\alpha} = \int \rho_{mn}(\mathbf{x})v_{\alpha}(\mathbf{x})d^3\mathbf{x} \tag{26}$$

$$= \int \eta_{mn,\alpha}(\mathbf{x})d^3\mathbf{x}. \tag{27}$$

The rate of internal conversion depends on the off-diagonal VCCs.

2.5 Transition Dipole Moment Density

The electric dipole moment operator $\hat{\mu}$ is defined by

$$\hat{\mu} = -\sum_i e\mathbf{r}_i. \tag{28}$$

The transition dipole moment μ_{mn} is given by

$$\mu_{mn} = \langle \Psi_m(\mathbf{r},\mathbf{R}_0)|\hat{\mu}|\Psi_n(\mathbf{r},\mathbf{R}_0)\rangle. \tag{29}$$

The oscillator strength f_{mn} is defined as follows[46]:

$$f_{mn} = \frac{2m_e}{3\hbar^2 e^2}(E_n - E_m)|\mu_{mn}|^2, \tag{30}$$

where m_e denotes the mass of an electron, and E_m denotes the eigenenergy for the electronic state S_m.

Fluorescence decay obeys the formula for the rate constant of spontaneous emission described by[43]

$$k_{m\to n}^{\mathrm{F}}(T) = \int_0^\infty d\omega \frac{4\omega^3}{3c^3}\sum_{ij}P_{mi}(T)|\mu_{nm}|^2|\langle\chi_{nj}|\chi_{mi}\rangle|^2\delta(\hbar\omega - E_{mi} + E_{nj}), \tag{31}$$

where $\hbar\omega$ denotes a photon energy and $|\langle\chi_{nj}|\chi_{mi}\rangle|^2$ denotes the Franck–Condon factor, and E_{mi} and E_{nj} denote the eigenenergies for the vibronic states. Using Eqs. (12) and (31), we can obtain the formula of the fluorescence quantum yield described by

12

$$\Phi^{\mathrm{F}}_{m\to n}(T) = \frac{k^{\mathrm{F}}_{m\to n}(T)}{k^{\mathrm{IC}}_{m\to n}(T) + k^{\mathrm{F}}_{m\to n}(T)} \tag{32}$$

$$= \frac{\sum_{ij} P_{mi}(T) \int_0^\infty 4\omega^3 \hbar |\mu_{nm}|^2 |\langle \chi_{nj}|\chi_{mi}\rangle|^2 \delta(\hbar\omega - E_{mi} + E_{nj})\, d\omega}{\sum_{ij} P_{mi}(T) \left[\int_0^\infty 4\omega^3 \hbar |\mu_{nm}|^2 |\langle \chi_{nj}|\chi_{mi}\rangle|^2 \delta(\hbar\omega - E_{mi} + E_{nj})\, d\omega + 6\pi c^3 \sum_{\alpha\beta} V_{nm,\alpha} V_{mn,\beta} \langle \chi_{nj}|Q_\alpha|\chi_{mi}\rangle \langle \chi_{mi}|Q_\beta|\chi_{nj}\rangle \delta(E_n - E_m - \hbar\omega_{ij}) \right]}, \tag{33}$$

13

indicating that the fluorescence quantum yield is large when the rate constant of fluorescence is large. Thus, a strong transition dipole moment directly enhances the quantum yield.

The transition dipole moment density (TDMD)[40] is defined as follows:

$$\tau_{mn} = -e\mathbf{x}\,\rho_{mn}(\mathbf{x}).\tag{34}$$

Note that the origin of position vector $\mathbf{x}$ for a transition dipole moment is allowed to be set anywhere, which is different from the case of a permanent dipole moment. We set the origin of $\mathbf{x}$ at the centre of the charges in the anthracenylene groups in the TDMD analyses.

The integral of τ_{mn} is equal to the transition dipole moment μ_{mn}:

$$\mu_{mn} = \int \tau_{mn}\,d^3\mathbf{x}.\tag{35}$$

The TDMD provides a local picture of a transition dipole moment. A widespread distribution of the overlap density can yield a large dipole moment.

3   Method of Calculation

We calculated the electronic structures of MADN, MAM, MAT, and TAT in the S_0, FC S_1 and AD S_1 states and the vibrational structures of the molecules for the S_0 states. The calculations were performed by employing the B3LYP/6-31G(d) level of theory. The excited states were calculated using the time-dependent density functional theory (TD-DFT). The Gaussian 09 program[47] was used for the computation; VCCs, VCDs, and TDMDs were calculated with our codes.

3.1   Ground State

We optimized the structures of MADN, MAM, MAT and TAT in the S_0 state. We also confirmed whether the optimized structures of the molecules are in local minima through vibrational analyses.

3.2 Franck–Condon S_1 State

The forces in the FC S_1 states were calculated. The diagonal VCCs in the FC S_1 states were calculated using the matrix elements of the force matrices and the normal modes obtained from the vibrational analyses. The VCDs of the maximum-coupling modes for the FC S_1 states were also calculated.

3.3 Adiabatic S_1 State

We also optimized the structures for the S_1 states in order to obtain the AD S_1 state. The normal modes employed for the off-diagonal VCC and VCD calculations were obtained from the vibrational analyses for the S_0 state at the optimized structures of the S_1 state. We calculated the off-diagonal VCCs between the S_1 and S_0 states at the optimized structures in the S_1 state from Eq.(27) by using the electronic wavefunctions and the normal modes obtained above.

VCD analyses between the S_1 and S_0 states were applied for the maximum-coupling modes of the AD S_1 states.

The transition dipole moments between the S_1 and S_0 states were also analyzed in terms of the TDMD for the AD S_1 state.

4 Results and Discussion

4.1 Transition Energies and Oscillator Strengths

The change in the optimized structures of MADN between the S_1 and S_0 states are shown in Fig. 1e, with an illustration of the torsional angles between the planes of the core moiety (2-methyl-9,10-anthracenylene group) and the side moiety (2-naphthalenyl group), θ_1 and θ_2. The torsional angles θ_1 and θ_2 for the FC S_1 state are larger than those for the AD S_1 state. The torsional angles of the four molecules are summarized in Table 1. The side groups of the four

15

molecules are twisted after vibrational relaxation in the FC S_1 state.

The transition energies E and the oscillator strengths f in the FC and AD S_1 states are listed in Table 2. The calculated transition energies in the FC S_1 states are in good agreement with the experimental absorption wavelengths. The calculated transition energies in the AD S_1 state are about 10% smaller than the experimental fluorescence wavelengths. It should be noted that the f values are enhanced after vibrational relaxation, especially for TAT. The calculated f values in the AD S_1 state are in the order MAM < MAT < TAT, which is consistent with the order of the experimental PL quantum yield for these three molecules. Although MADN has a larger f than does MAM, the PL quantum yield for MADN is smaller than that for MAM.

4.2   Vibronic Coupling Constants in the Franck–Condon State

The VCCs in the FC S_1 states are shown in Figs. 3. The most intense VCC peaks appear at around 1600 cm^{-1}. The VCCs for the maximum-coupling modes are almost the same. The maximum-coupling mode for MADN is shown in Fig. 4a, which is similar to that for the other molecules. The maximum-coupling modes correspond to the C–C stretching mode localized on the core moiety (9,10-anthracenylene group). This shows that electrons of the four molecules after the vertical excitation couple strongly with the C–C stretching mode and the structural deformation along this mode is large. Therefore, the maximum-coupling C–C stretching mode has large reorganization energy and is the main target to be reduced for efficiency.

Figure 5 shows the reorganization energies ΔE for MADN, MAM, MAT, and TAT. The low-frequency modes (below 15 cm^{-1}) correspond to the torsional modes in the plane of the side moieties. The adiabatic potentials for the torsional modes are not harmonic (see Section 4.4 and Section S3 in the ESI). For this reason, the reorganization energies for these low-frequency modes are calculated by taking the anharmonicity into consideration. The corrections for ΔE are performed by following the potential surfaces along the low-frequency modes. These potential surfaces are shown in Section 4.4 and Section S3 in the ESI.

16

The reorganization energy using the CA approximation with the low-frequency mode correction ΔE_{CA}, the reorganization energy using the BO approximation ΔE_{BO}, and Stokes shifts E^{St} are listed in Table 3. ΔE_{CA} is in good agreement with ΔE_{BO}, indicating that the harmonic approximation is valid, except for the low-frequency modes. Although ΔE_{CA} is calculated using the frequencies in the S_0 state instead of those in the S_1 state, it is nearly equal to ΔE_{BO}. This suggests that the curvatures at the minimum of the adiabatic potential for the S_1 state are not much different from those for the S_0 state.

The calculated Stokes shifts were estimated from the reorganization energies. The experimental Stokes shifts are smaller than the calculated ones by around 0.3 eV, as tabulated in Table 3. The calculated transition energies for the FC S_1 state are larger than the experimental absorption maximum energies by approximately 0.1 eV, and the calculated transition energies for the AD S_1 state are smaller than the experimental emission maximum energies by approximately 0.2 eV. As evident from Table 3, the calculated E^{St} for MAM is the smallest, and the other calculated E^{St} is almost the same. The calculated reorganization energies are consistent with the Stokes shifts obtained from the experiment.

From Fig. 5, it is seen that MAM has the smallest ΔE because of the smallest number of the active modes. According to the selection rule for a vibronic coupling, the vibronic active modes are totally symmetric. All the 171 modes are active in MADN because of the C_1 symmetry:

$$\Gamma(C_1\text{-MADN}) = 171A \tag{36}$$

For MAM, which shows D_2 symmetry, on the other hand, 61 modes among the total 246 modes are vibronically active:

$$\Gamma(D_2\text{-MAM}) = 61A + 59B_1 + 63B_2 + 63B_3. \tag{37}$$

The number of active modes in MAM is smaller than that in MADN. As a result, MAM has a smaller ΔE than does MADN. This suggests that MAM is more efficient than MADN.

As shown in Fig. 5, the contribution of the maximum-coupling mode to ΔE is the largest in each molecule. The reorganization energies for the maximum-coupling mode are almost the same. In order to design a novel molecule with low energy dissipation, it is crucial to reduce the reorganization energies for the maximum-coupling modes. VCD analysis for the maximum-coupling mode will be helpful to investigate why these molecules have almost the same VCCs for the maximum-coupling mode. The following subsection shows the analysis of the maximum-coupling mode of MADN in terms of the VCD.

4.3 Vibronic Coupling Density in the Franck–Condon State

Figure 4b shows the potential derivatives v_α with respect to the maximum-coupling mode. The potential derivative is localized on the 9,10-anthracenylene group. Figure 4c shows the electron density difference between the S_1 and S_0 states, $\Delta\rho_1$. The electron density difference is localized on the anthracenylene group. Therefore, v_α effectively overlaps with $\Delta\rho_1$ on the core moiety. Accordingly, the vibronic coupling density $\eta_{1,\alpha}$ is localized on the anthracenylene group, as shown in Figure 4d. The four molecules have the similar distribution of v_α, $\Delta\rho_1$, and $\eta_{1,\alpha}$. Hence, the diagonal VCCs for the maximum-coupling modes are almost the same.

It is found that the vibronic couplings in the FC S_1 state originate from the core moiety because $\Delta\rho_1$ is localized on the anthracenylene group. For the molecular design with low energy loss, $\Delta\rho_1$ on the core moiety should be reduced. The torsional distortion of the side groups in the FC S_1 is caused by the overlap between $\Delta\rho_1$ and v_α for the low-frequency torsional modes (see the following subsection). Because the vibration relaxation in the low-frequency mode is crucial, as discussed later, we investigate the origin of the torsional distortion by VCD analysis.

18

4.4 Diagonal Vibronic Coupling Density Analysis in the Lowest-frequency Torsional Mode

The lowest-frequency torsional mode for TAT is shown in Fig. 7a. The lowest-frequency mode is an intramolecular rotation of the side moieties with respect to the C(9) and C(10) axes.

In order to discuss the role of the low-frequency mode in TAT, we define the torsional angle of the side groups θ with respect to the C(9)–C(10) axis, as illustrated in Fig. 6a. Note that $\theta = 0$ corresponds to the structures of the FC S_1 states in which the core anthracenylene plane and side adjacent phenylene planes are not perpendicular. The adiabatic potential energy curves for the S_1 and S_0 states as a function of the twist angle θ are shown in Fig. 6b. The potential energy curve for the S_0 state indicates a shallow potential with a small reorganization energy for the low-frequency torsional modes λ_θ. The twisted structures in the S_0 states can be ascribed to the pseudo Jahn–Teller effect[48].

On the other hand, the FC S_1 state gives rise to the reorganization energy, $\lambda_\theta = 0.087$ eV. The driving force of the vibrational relaxation in the FC S_1 state is the diagonal VCC.

We now focus on the VCD analysis for the diagonal VCC in the FC S_1 state of TAT. Figure 7b shows the derivative of the nuclear-electronic potential with respect to the lowest-frequency mode v_1 for TAT. The electron density difference $\Delta\rho_1$ for TAT is similar to that for MADN, as shown in Fig. 7c. Because the vibrational vector is localized on the side moieties ($3',5'$-diphenylbiphenyl-4-yl groups), v_1 for the side moieties is large. The diagonal vibronic coupling density for the lowest-frequency mode $\eta_{1,1}$ is shown in Fig. 7d. $\eta_{1,1}$ is small because of the small overlap between $\Delta\rho_1$, which is localized on the core moiety, and v_1, which is localized on the side moieties. Moreover, the vibronic coupling density $\eta_{1,1}$ on the core moiety is antisymmetric with respect to the anthracenylene plane. This distribution causes cancellation in the spatial integration of $\eta_{1,1}$. Therefore, the VCC for the lowest-frequency mode $V_{1,1}$ ($= 1.778 \times 10^{-6}$ a.u.) is much smaller than that for the maximum-coupling mode $V_{1,298}$ ($= 5.544 \times 10^{-4}$ a.u.)

The large λ_θ can be responsible for the higher order of the vibronic couplings. Though the VCC for the lowest-frequency mode is small, the finite VCC gives rise to torsional distortion in the FC S_1 state.

The VCC can be decomposed into atomic vibronic coupling constants (AVCCs).[36] The C(15)–C(18) atoms, which are indicated by arrows in Fig. 7d, have the largest diagonal AVCCs in the lowest-frequency mode, 0.518×10^{-6} a.u. This is because the distribution of $\eta_{1,1}$ on the C(15)–C(18) atoms is large and asymmetric. In addition, the small $\Delta\rho_1$ on the C(15)–C(18) atoms can overlap with ν_1 on the C(15)–C(18) atoms. The small portion of $\Delta\rho_1$ on the C(15)–C(18) atoms comes from the equilibrium structure in the ground S_0 state, which is slightly twisted from the orthogonal orientation between the planes of the core and side groups.

This suggests that a slightly twisted structure in the S_0 state gives rise to an asymmetric increase in $\Delta\rho_1$ on the C(15)–C(18) atoms and the distribution of $\Delta\rho_1$ should result in an increase in the torsion angle in the S_1 state, which can enhance the radiative transition, as discussed later.

4.5 Off-Diagonal Vibronic Coupling Constants

Off-diagonal vibronic couplings give rise to internal conversion, which leads to radiationless transitions. The off-diagonal VCCs between the S_0 and S_1 states are shown in Fig. 8. The maximum-coupling modes for MADN, MAT, and TAT correspond to the second maximum coupling mode for MAM. The order of the VCCs in atomic unit for these modes is as follows: MADN (1.92×10^{-4}) < MAT (2.51×10^{-4}) < MAM (3.38×10^{-4}) < TAT (3.49×10^{-4}). MADN has the smallest off-diagonal VCC for the maximum-coupling mode among the four molecules.

To calculate the rate of internal conversion, we should consider all the active modes. The number of active modes in MADN is the largest of the four, and hence, the rate of internal conversion for MADN should be large.

To suppress the internal conversion, the off-diagonal VCCs should be reduced. MADN has

the smallest off-diagonal VCC, and TAT has the largest off-diagonal VCC for the maximum-coupling mode among the four molecules. As the result of the VCD analyses for these modes, the off-diagonal VCDs $\eta_{01,\alpha}$ are localized on the core anthracenylene groups. This is due to the localized overlap densities ρ_{01}. The cancellation in the spatial integration of $\eta_{01,\alpha}$ makes difference in the values of $V_{01,\alpha}$. The details are discussed in the Section S2 in the ESI.

The vibronic coupling originates from the core anthracenylene group, as is the case in the diagonal VCD analysis in the FC S_1 state. Therefore, reducing the overlap density ρ_{01} on the core moiety is important to improve the quantum yield.

4.6   Transition Dipole Moment Density

A large transition dipole moment enhances the radiative process. The transition dipole moments increase after vibrational relaxations. In the AD S_1 states, the side groups are twisted after vibrational relaxations in the FC S_1 states. In order to clarify the structural dependence of the oscillator strengths, we calculated the oscillator strengths as a function of θ with respect to the C(9)–C(10) axes defined in Fig. 6a. Figure 9 shows the θ dependencies of f for the four molecules. The oscillator strengths f are at minimum around $\theta = 10°$ and become remarkably large with an increase in θ for $\theta > 20°$. In other words, the torsional deformation enhances the oscillator strength f. It should be noted that TAT has the largest f for any value of θ.

The θ dependence of the transition energies is almost the same, implying that the transition dipole moments increase with increasing θ.

We analyze the transition dipole moments by using the TDMD concept in order to explain why the transition dipole moments increase with increasing θ, especially in TAT. Figure 10 shows the overlap densities between the S_1 and S_0 states, ρ_{01}, for the FC and AD S_1 structures of TAT. ρ_{01} at the edges becomes slightly large after vibrational relaxation, as indicated by the two red arrows in Fig. 10b. It is important to note that the distance between the edges indicated by the red arrows is as long as about 20.1 Å.

In the calculation of TDMD, we set the centre of the charges on the anthracenylene groups as the origin. The z-axis is taken along the direction between the C(9) and C(10) atoms, as shown in Fig. 1. The z-component of the transition dipole moment densities, $\tau_{01,z}$, for TAT in the FC and AD S_1 states are depicted in Fig. 11. $\tau_{01,z}$ at the edges of the molecule increases remarkably owing to the increase in ρ_{01} at the edges with the large molecular size.

Figure 10 indicates that ρ_{01} is small on the side $3', 5'$-diphenylbiphenyl-4-yl groups. However, $\tau_{01,z}$ on the side moieties is large because the z-component of the position vector **x** is large at the edges. TAT has a large $\tau_{01,z}$ at the edges because of the long distance between the two edges.

The transition dipole moments can be decomposed into atomic transition dipole moments (ATDMs)[40]. The sum of the z-component of the ATDMs on the side and core moieties is tabulated in Table 4. The transition dipole moments for the side moieties are larger than those for the core moiety, and the contributions from the side moieties become large after vibrational relaxation, especially in TAT. This result is consistent with the distribution of $\tau_{01,z}$. The torsional distortion after vibrational relaxation in the FC S_1 state gives rise to the strong fluorescence because of enhancement of the transition dipole moments for the side moieties. TAT is such a long molecule that the transition dipole moment is strongly enhanced because of the contributions from the side moieties after vibrational relaxation.

The off-diagonal vibronic couplings between the S_1 and S_0 states mainly come from the core moieties because ρ_{01}'s are localized on the anthracenylene groups (Figure S6). On the other hand, the z-components of the transition dipole moments are enhanced on the side moieties because ρ_{01}'s for the AD states are distributed on the edges. Therefore, the design principles for an efficient emitting molecule are to reduce ρ_{01} on the anthracenylene group and to increase ρ_{01} at the edges.

22

5   Conclusion

The reorganization energies ΔE calculated from the diagonal VCCs in the FC S_1 states are consistent with the experimental values of the Stokes shifts. The reorganization energy ΔE for MAM is the smallest among the four molecules because of the least number of active modes. This is also important for the off-diagonal vibronic couplings because the internal conversion should be suppressed. This suggests that PL yield for MAM can be larger than that for MADN. By using the VCD concept, we have revealed that the vibronic couplings in the FC states mainly come from the core moieties because the electron density differences $\Delta \rho_1$ are localized on the anthracenylene groups.

The off-diagonal vibronic couplings between the S_1 and S_0 states in the structures of the AD S_1 states also mainly originate from the core moieties in all the molecules considered, because of the large overlap densities ρ_{01} on the anthracenylene groups. As a result, the vibronic couplings are similar in the four molecules.

On the other hand, the transition dipole moments are enhanced in the side moieties after the vibrational relaxations originating from the diagonal VCC for the torsional mode in the FC S_1 state. The driving force of the diagonal VCC for the torsional mode that results in the greatly twisted structure in the AD S_1 state comes from the small portion of the electron density difference on the side moieties due to the slightly twisted structure in the FC S_1 state. Because the torsional angle is large in TAT, this molecule shows strong transition dipole moment densities at the edges. Hence, TAT has the largest transition dipole moment.

Finally, the design principles to enhance quantum yields in anthracene derivatives are as follows: (1) reduction in $\Delta \rho_1$ and ρ_{01} in the core moiety and (2) increase in ρ_{01} in the side moieties. The twisted symmetry-broken structures in the S_0 state are crucial to enhance the transition dipole moments.

For example, in an anthracene derivative, the design principles suggest that the overlap be-

23

tween the π and π^* orbitals should be reduced in the anthracene moiety and be increased in the side moieties. This can be achieved by the delocalization of these orbitals. The extension of π conjugation to side moieties is preferable. In addition, the number of active modes in vibronic couplings should be reduced in order to suppress internal conversion. Therefore, molecules should be keep as high symmetry of the anthracene, D_{2h}, as possible. For instance, if two longer rigid π-conjugated side groups than the $3',5'$-diphenylbiphenyl-4-yl group of TAT are introduced to the C(9) and C(10) positions of the anthracene, if possible, keeping the D_{2h} symmetry, the molecule can be expected to exhibit a higher quantum yield than TAT.

The symmetry breaking can be ascribed to the pseudo Jahn–Teller effect. A novel emitting molecule designed on the basis of the aforementioned principles is under investigation. The results will be published in the near future.

Acknowledgement

References

[1] C. W. Tang and S. A. Van Slyke, *Appl. Phys. Lett.*, 1987, **51**, 913–915.

[2] C. Adachi, T. Tsutsui and S. Saito, *Appl. Phys. Lett.*, 1989, **55**, 1489–1491.

[3] R. H. Friend, R. W. Gymer, A. B. Holmes, J. H. Burroughes, R. N. Marks, C. Taliani, D. D. C. Bradley, D. A. D. Santos, J. L. Brédas, M. Löglund and W. R. Salaneck, *Nature*, 1999, **397**, 121–128.

[4] M. A. Baldo, M. E. Thompson and S. R. Forrest, *Nature*, 2000, **403**, 750–753.

[5] L. S. Hung and C. H. Chen, *Mater. Sci. Eng. R*, 2002, **39**, 143–222.

[6] B. W. D'Andrade and S. R. Forrest, *Adv. Mater.*, 2004, **16**, 1585–1595.

[7] C.-C. Wu, Y.-T. Lin, K.-T. Wong, R.-T. Chen and Y.-Y. Chien, *Adv. Mater.*, 2004, **16**, 61–65.

[8] R. J. Tseng, R. C. Chiechi, F. Wudl and Y. Yang, *Appl. Phys. Lett.*, 2006, **88**, 093512(1–3).

[9] T. Arakane, M. Funahashi, H. Kuma, K. Fukuoka, K. Ikeda, H. Yamamoto, F. Moriwaki and C. Hosokawa, *SID Int. Symp. Digest Tech. Papers*, 2006, **37**, 37–40.

[10] B.-J. Jung, J.-I. Lee, H. Y. Chu, L.-M. Do, J. Lee and H.-K. Shim, *J. Mater. Chem.*, 2005, **15**, 2470–2475.

[11] Y. S. Yao, Q. X. Zhou, X. S. Wang, Y. Wang and B. W. Zhang, *J. Mater. Chem.*, 2006, **16**, 3512–3520.

[12] T. Tsuzuki and S. Tokito, *Adv. Mater.*, 2007, **19**, 276–280.

[13] K. T. Kamtekar, C. Wang, S. Bettington, A. S. Batsanov, I. F. Perepichka, M. R. Bryce, J. H. Ahn, M. Rabinal and M. C. Petty, *J. Mater. Chem.*, 2006, **16**, 3823–3835.

[14] M. Cocchi, D. Virgili, V. Fattori, D. L. Rochester and J. A. G. Williams, *Adv. Funct. Mater.*, 2007, **17**, 285–289.

[15] C. Hosokawa, H. Higashi, H. Nakamura and T. Kusumoto, *Appl. Phys. Lett.*, 1995, **67**, 3853–3855.

[16] J. Shi and C. W. Tang, *Appl. Phys. Lett.*, 2002, **80**, 3201–3203.

[17] M.-T. Lee, H.-H. Chen, C.-H. Liao and C.-H. Tsai, *Appl. Phys. Lett.*, 2004, **85**, 3301–3303.

[18] C.-H. Chen, F.-I. Wu, C.-F. Shu, C.-H. Chien and Y.-T. Tao, *J. Mater. Chem.*, 2004, **14**, 1585–1589.

[19] X. Ren, J. Li, R. J. Holmes, P. I. Djurovich, S. R. Forrest and M. E. Thompson, *Chem. Mater.*, 2004, **16**, 4743–4347.

[20] S.-W. Wen, M.-T. Lee and C. H. Chen, *J. Display Tech.*, 2005, **1**, 90–99.

[21] M.-T. Lee, C.-H. Liao, C.-H. Tsai and C. H. Chen, *Adv. Mater.*, 2005, **17**, 2493–2497.

[22] M.-H. Ho, Y.-S. Wu, S.-W. Wen, M.-T. Lee, T.-M. Chen, C. H. Chen, K.-C. Kwok, S.-K. So, K.-T. Yeung, Y.-K. Cheng and Z.-Q. Gao, *Appl. Phys. Lett.*, 2007, **89**, 252903(1–3).

[23] Z. Q. Gao, B. X. Mi, C. H. Chen, K. W. Cheah, Y. K. Cheng and W.-S. Wen, *Appl. Phys. Lett.*, 2007, **90**, 123506(1–3).

[24] J. H. Ahn, C. Wang, I. F. Perepichka, M. R. Bryce and M. C. Petty, *J. Mater. Chem.*, 2007, **17**, 2996–3001.

[25] Y.-Y. Lyu, J. Kwak, O. Kwon, S.-H. Lee, D. Kim, C. Lee and K. Char, *Adv. Mater.*, 2008, **20**, 2720–2729.

[26] L. Wang, Z.-Y. Wu, W.-Y. Wong, K.-W. Cheah, H. Huang and C. H. Chen, *Org. Electron.*, 2011, **12**, 595–601.

[27] S. Wang, W. J. Oldham Jr., R. A. Hudack Jr. and G. Bazan, *J. Am. Chem. Soc.*, 2000, **122**, 5695–5709.

[28] S.-K. Kim, B. Yang, Y. Ma, J.-H. Lee and J.-W. Park, *J. Mater. Chem.*, 2008, **18**, 3376–3384.

[29] D. Yokoyama, Y. Park, B. Kim, S.-K. Kim, Y.-J. Pu, J. Kido and J.-W. Park, *J. Mater. Chem.*, 2008, **18**, 3376(1–3).

[30] K. Shizu, T. Sato and K. Tanaka, *Nanoscale*, 2010, **2**, 2186–2194.

[31] M. Bixon and J. Jorter, *J. Chem. Phys.*, 1968, **15**, 715–726.

[32] R. Islampour and M. Miralinaghi, *J. Phys. Chem. A*, 2007, **111**, 9454–9462.

[33] K. Gustav and M. Storch, *Int. J. Quantum. Chem.*, 1990, **38**, 1–10.

[34] M. Hayashi and A. M. Mebel, *J. Chem. Phys.*, 1998, **108**, 2044–2055.

[35] T. Sato, K. Tokunaga and K. Tanaka, *J. Phys. Chem. A*, 2008, **112**, 758–767.

[36] T. Sato, K. Shizu, T. Kuga, K. Tanaka and H. Kaji, *Chem. Phys. Lett.*, 2008, **458**, 152–156.

[37] T. Sato, K. Tokunaga, N. Iwahara, K. Shizu and K. Tanaka, in *The Jahn–Teller Effect: Fundamentals and Implications for Physics and Chemistry*, ed. H. Köppel, D. R. Yarkony and H. Barentzen, Springer–Verlag, Berlin and Heidelberg, 2009, pp. 99–129.

[38] K. Shizu, T. Sato, K. Tanaka and H. Kaji, *J. Mater. Chem.*, 2011, **21**, 6375–6382.

[39] K. Shizu, T. Sato, K. Tanaka and H. Kaji, *Appl. Phys. Lett.*, 2010, **97**, 142111(1–3).

[40] T. Sato, M. Uejima, N. Iwahara, N. Haruta, K. Shizu and K. Tanaka, *J. Phys.: Conf. Ser.*, 2013, **428**, 012010(1–19).

[41] M. Uejima, T. Sato, K. Tanaka and H. Kaji, *Chem. Phys.*, 2014, **430**, 47–55.

[42] G. Fischer, *Vibronic Coupling: The Interaction Between the Electronic and Nuclear Motions*, Academic Press, London, 1984.

[43] Y. Niu, Q. Peng, C. Deng, X. Gao and Z. Shuai, *J. Phys. Chem. A*, 2010, **114**, 7817–7831.

[44] E. Hucthisson, *Phys. Rev.*, 1930, **36**, 410.

[45] K. Shizu, T. Sato, K. Tanaka and H. Kaji, *Org. Electron.*, 2010, **11**, 1277–1287.

[46] R. C. Hilborn, *Am. J. Phys.*, 1982, **50**, 982–986.

[47] M. J. Frisch, G. W. Trucks, H. B. Schlegel, G. E. Scuseria, M. A. Robb, J. R. Cheeseman, G. Scalmani, V. Barone, B. Mennucci, G. A. Petersson, H. Nakatsuji, M. Caricato, X. Li, H. P. Hratchian, A. F. Izmaylov, J. Bloino, G. Zheng, J. L. Sonnenberg, M. Hada, M. Ehara, K. Toyota, R. Fukuda, J. Hasegawa, M. Ishida, T. Nakajima, Y. Honda, O. Kitao, H. Nakai, T. Vreven, J. A. Montgomery, Jr., J. E. Peralta, F. Ogliaro, M. Bearpark, J. J. Heyd, E. Brothers, K. N. Kudin, V. N. Staroverov, R. Kobayashi, J. Normand, K. Raghavachari, A. Rendell, J. C. Burant, S. S. Iyengar, J. Tomasi, M. Cossi, N. Rega, J. M. Millam, M. Klene, J. E. Knox, J. B. Cross, V. Bakken, C. Adamo, J. Jaramillo, R. Gomperts, R. E. Stratmann, O. Yazyev, A. J. Austin, R. Cammi, C. Pomelli, J. W. Ochterski, R. L. Martin, K. Morokuma, V. G. Zakrzewski, G. A. Voth, P. Salvador, J. J. Dannenberg, S. Dapprich, A. D. Daniels, Ö. Farkas, J. B. Foresman, J. V. Ortiz, J. Cioslowski and D. J. Fox, *Gaussian 09 Revision B.1*, Gaussian, Inc., Wallingford, CT, 2009.

[48] I. B. Bersuker and V. Z. Polinger, *Vibronic Interactions in Molecules and Crystals*, Springer–Verlag, Berlin and Heidelberg, 1989.

Table 1: Torsional angles θ_1 and θ_2 of MADN, MAM, MAT, and TAT. FC and AD indicate the Franck–Condon S_1 state and adiabatic S_1 state, respectively.

Molecule	State	Point Group	θ_1	θ_2
MADN	FC	C_1	80.5	81.8
	AD	C_1	54.7	54.7
MAT	FC	D_2	85.4	85.4
	AD	D_2	58.9	58.9
MAT	FC	C_2	81.8	97.0
	AD	C_2	59.4	53.8
TAT	FC	D_2	80.1	80.1
	AD	D_2	54.3	54.3

Table 2: Transition energies E and oscillator strengths f between the S_1 and S_0 states. FC and AD indicate the Franck–Condon S_1 state and adiabatic S_1 state, respectively.

Molecule	State	E_{calc}		E_{exp}[a]	f
		(eV)	(nm)	(nm)	
MADN	FC	3.1422	394.59	405	0.2191
	AD	2.5322	489.64	447	0.3864
MAM	FC	3.1490	393.72	402	0.2324
	AD	2.6054	475.87	439	0.3241
MAT	FC	3.1477	393.88	403	0.2652
	AD	2.5582	484.66	445	0.4572
TAT	FC	3.1259	396.63	403	0.3253
	AD	2.5131	493.36	445	0.5981

[a] Ref. 28

Table 3: Corrected reorganization energies using the Born–Oppenheimer approximation ΔE_{BO} and using the crude adiabatic approximation ΔE_{CA} and Stokes shifts E_{BO}^{St}, E_{CA}^{St}, and E_{exp}^{St} calculated from ΔE_{BO}, ΔE_{CA}, and the experiment, respectively.

Molecule	ΔE_{BO}		E_{BO}^{St}	ΔE_{CA}		E_{CA}^{St}	E_{exp}^{St} [a]
	S_1	S_0		S_1	S_0		
MADN	0.3445	0.2654	0.6099	0.3139	0.2357	0.5496	0.29
MAM	0.2880	0.2556	0.5436	0.2595	0.2502	0.5097	0.26
MAT	0.3234	0.2661	0.5895	0.2950	0.2534	0.5484	0.28
TAT	0.3390	0.2738	0.6128	0.3240	0.2310	0.5550	0.28

[a] Ref. 28.

Table 4: Transition dipole moments for the core and the left/right-side moieties in atomic unit.

FC and AD indicate the Franck–Condon state and adiabatic state, respectively.

Molecule	State	Left	Core	Right	Total
MADN	FC	-0.631	-0.424	-0.632	-1.687
	AD	-1.094	-0.283	-1.117	-2.494
MAM	FC	-0.630	-0.477	-0.630	-1.737
	AD	-0.928	-0.396	-0.928	-2.253
MAT	FC	-0.820	-0.481	-0.552	-1.852
	AD	-1.437	-0.343	-0.920	-2.701
TAT	FC	-0.737	-0.475	-0.737	-1.949
	AD	-1.412	-0.293	-1.412	-3.118

Figure Captions

Fig. 1: Chemical structures of bulky-side anthracenes: (a) 2-methyl-9,10-di(2′-naphthyl)anthracene (MADN); (b) 4,9,10-bis(3′,5′-diphenylphenyl)anthracene (MAM); (c) 9-(3′,5′-diphenylphenyl)-10-(3″,5″-diphenylbiphenyl-4″-yl)anthracene (MAT); (d) 9,10-bis(3‴,5‴-diphenylbiphenyl-4′-yl)anthracene (TAT); and (e) optimized structure for MADN in the S_0 state and torsional angles between the planes of the core moiety and those of the side moiety, θ_1 and θ_2. The carbon atoms on the anthracenylene unit are labelled. The z-axis is defined along the direction between the C(9) and C(10) atoms.

Fig. 2: Dependence of rate constant of internal conversion on diagonal vibronic coupling constant, $V_{n,\alpha}$ and energy gap, $E_m - E_n$. Off-diagonal vibronic coupling constant is $V_{mn,\alpha} = 3 \times 10^{-4}$ a.u., and linewidth is $\sigma = 300$ cm^{-1}. Frequencies of the normal mode α are (a) 1400 cm^{-1} and (b) 1600 cm^{-1}.

Fig. 3: Diagonal vibronic coupling constants in the Franck–Condon S_1 state: (a) MADN, (b) MAM, (c) MAT, and (d) TAT.

Fig. 4: Diagonal vibronic coupling density analysis for MADN: (a) maximum-coupling mode ($\omega_{139} = 1612.22$ cm^{-1}); (b) derivative of the nuclear-electronic potential v_{139}; (c) electron density difference $\Delta\rho_1$; and (d) vibronic coupling density $\eta_{1,139}$. The isosurface values for v_{139}, $\Delta\rho_1$, and $\eta_{1,139}$ are 1×10^{-2}, 1×10^{-3}, and 5×10^{-6}, in atomic units. Blue regions are negative; white regions are positive.

Fig. 5: Corrected reorganization energies ΔE for the MADN, MAM, MAT, and TAT. '1st', '2nd', and '3rd' denote the contributions of modes ordered by their vibronic coupling constants. 'low-freq.' denotes the low-frequency modes less than 15 cm^{-1}.

33

Fig. 6: Potential energy curves for TAT: (a) twist angle of side moieties of the molecule from the structure of TAT in the Franck–Condon S_1 state, θ; and (b) potential energy curves as a function of θ for the S_1 and S_0 states. λ_θ represents the reorganization energy for the twist of the side groups.

Fig. 7: Diagonal vibronic coupling density analysis for TAT: (a) the lowest-frequency mode ($\omega_1 = 4.21$ cm^{-1}), from (a1) top view and (a2) side view; (b) derivative of the nuclear-electronic potential v_1; (c) electron density difference $\Delta\rho_1$ for the left side of molecule; and (d) vibronic coupling density $\eta_{1,1}$. The isosurface values for v_1, $\Delta\rho_1$, and $\eta_{1,1}$ are 5×10^{-3}, 1×10^{-3}, and 1×10^{-7}, in atomic units. Blue regions are negative; white regions are positive. The arrows indicate the carbon atoms with the largest atomic vibronic coupling constants.

Fig. 8: Off-diagonal vibronic coupling constants between the S_0 and S_1 states: (a) MADN, (b) MAM, (c) MAT, and (d) TAT.

Fig. 9: Oscillator strength dependence on the twist angle θ. θ is defined as the twist angle of the side moieties of the molecules from the structure in the Franck–Condon state, as shown in Fig. 6a.

Fig. 10: Overlap densities between the S_1 and S_0 states: (a) Franck–Condon state and (b) adiabatic state. The isosurface value is 1×10^{-3} a.u. Blue regions are negative; white regions are positive.
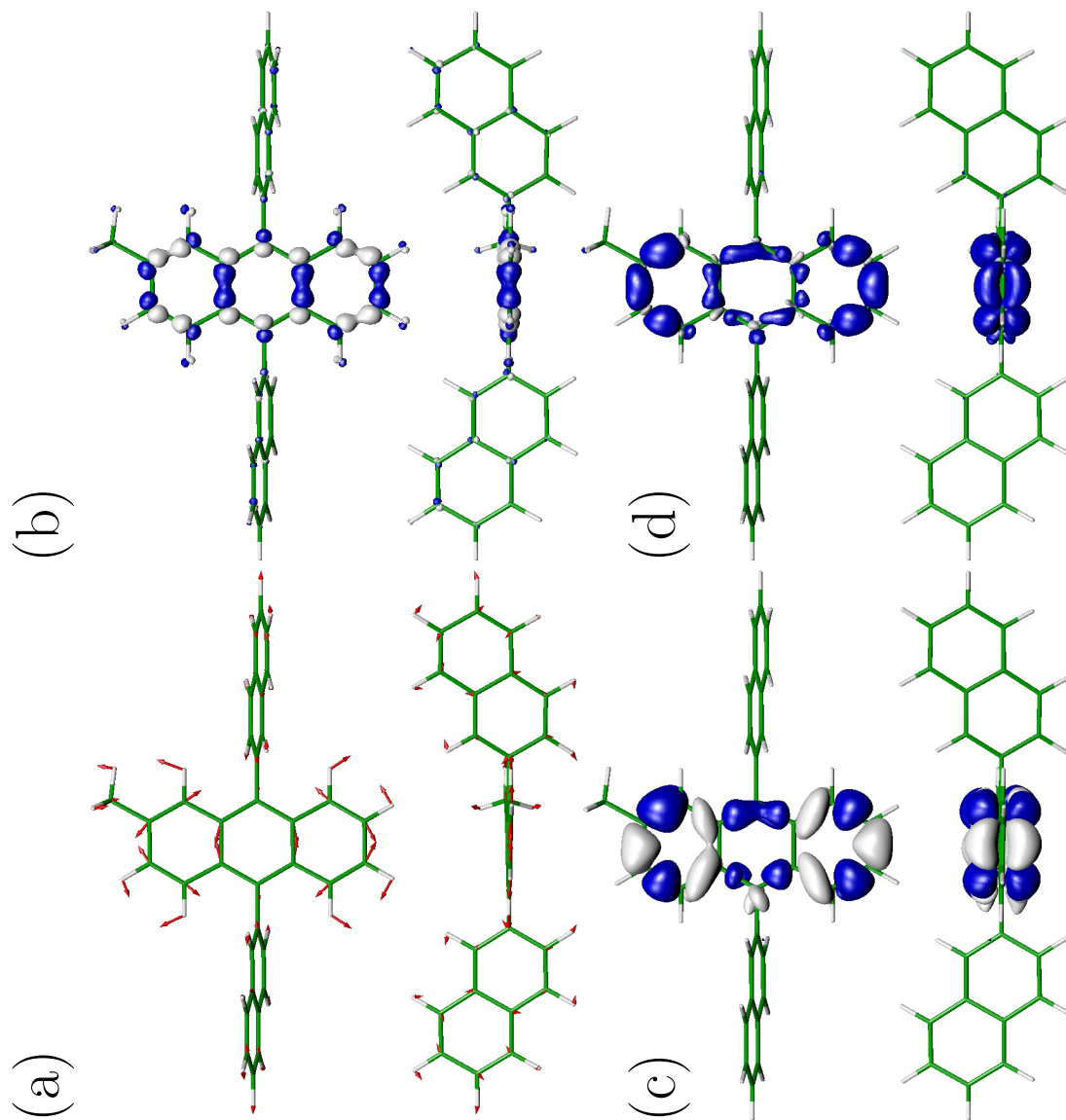
Fig. 11: Transition dipole moment densities between the S_1 and S_0 states: (a) Franck–Condon state and (b) adiabatic state. The origins of the position vectors are set at the centre of charges
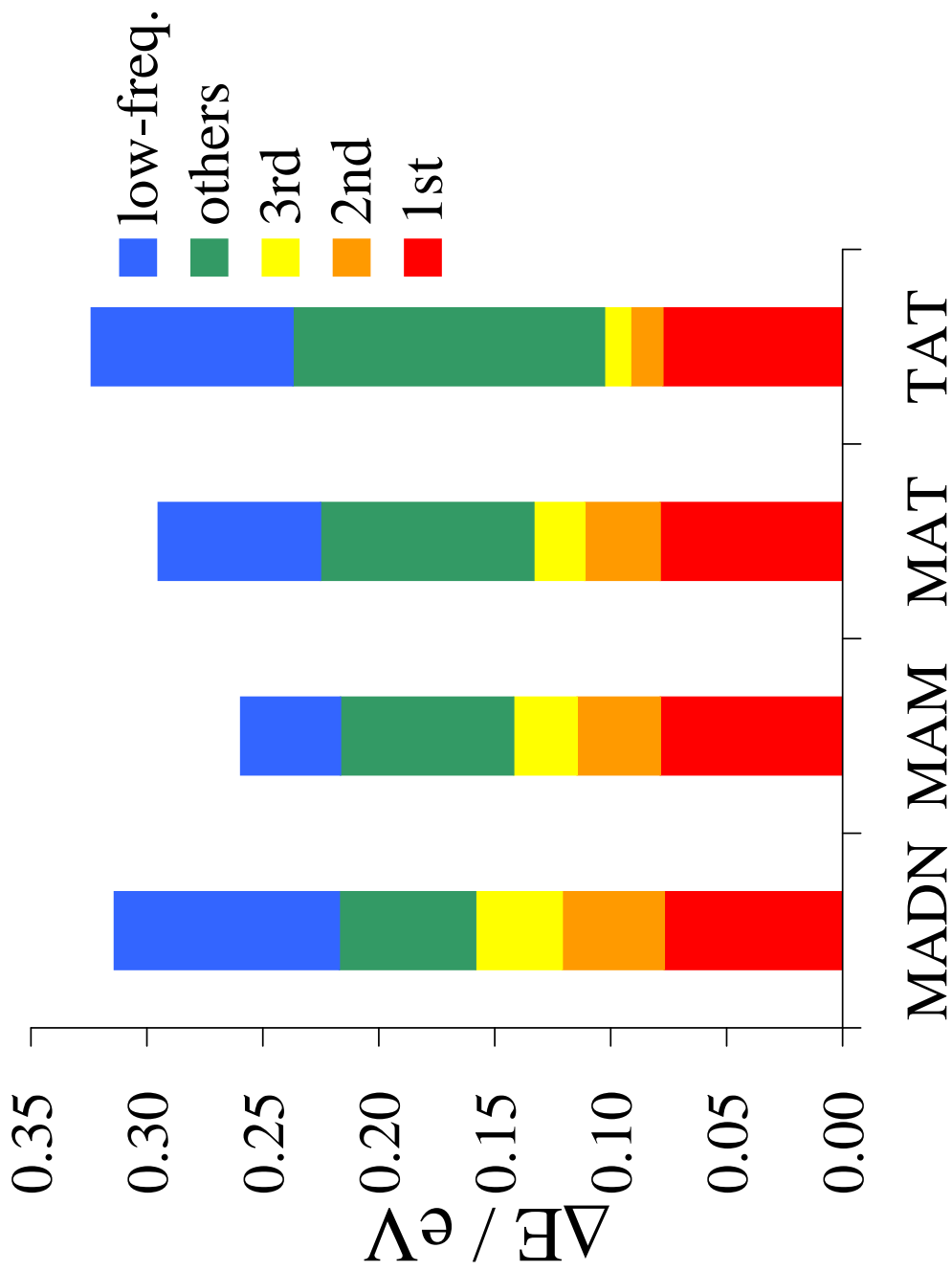
34

for the anthracenylene groups. The isosurface value is 1×10^{-3} a.u. Blue regions are negative;

white regions are positive.

(a) MADN

Me

3 2
4 1
12
11 9
10
14
5 13 8
6 7

(b) MAM

(c) MAT

(d) TAT

z

(e)

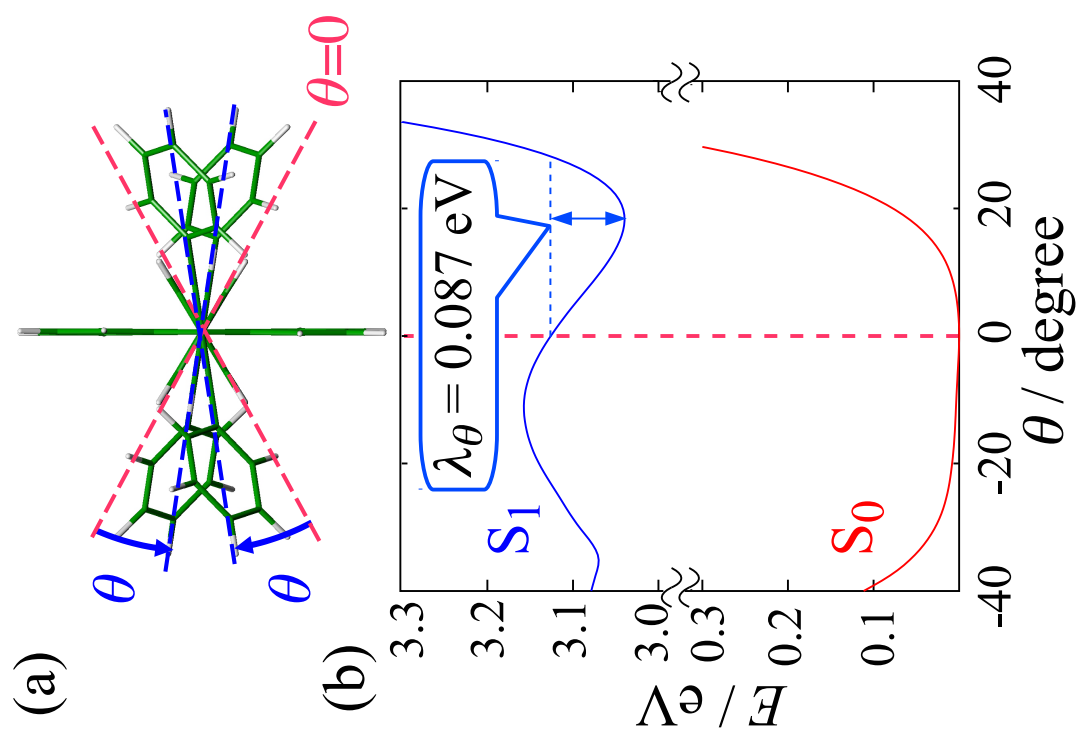θ_1 θ_2

θ_1 θ_2
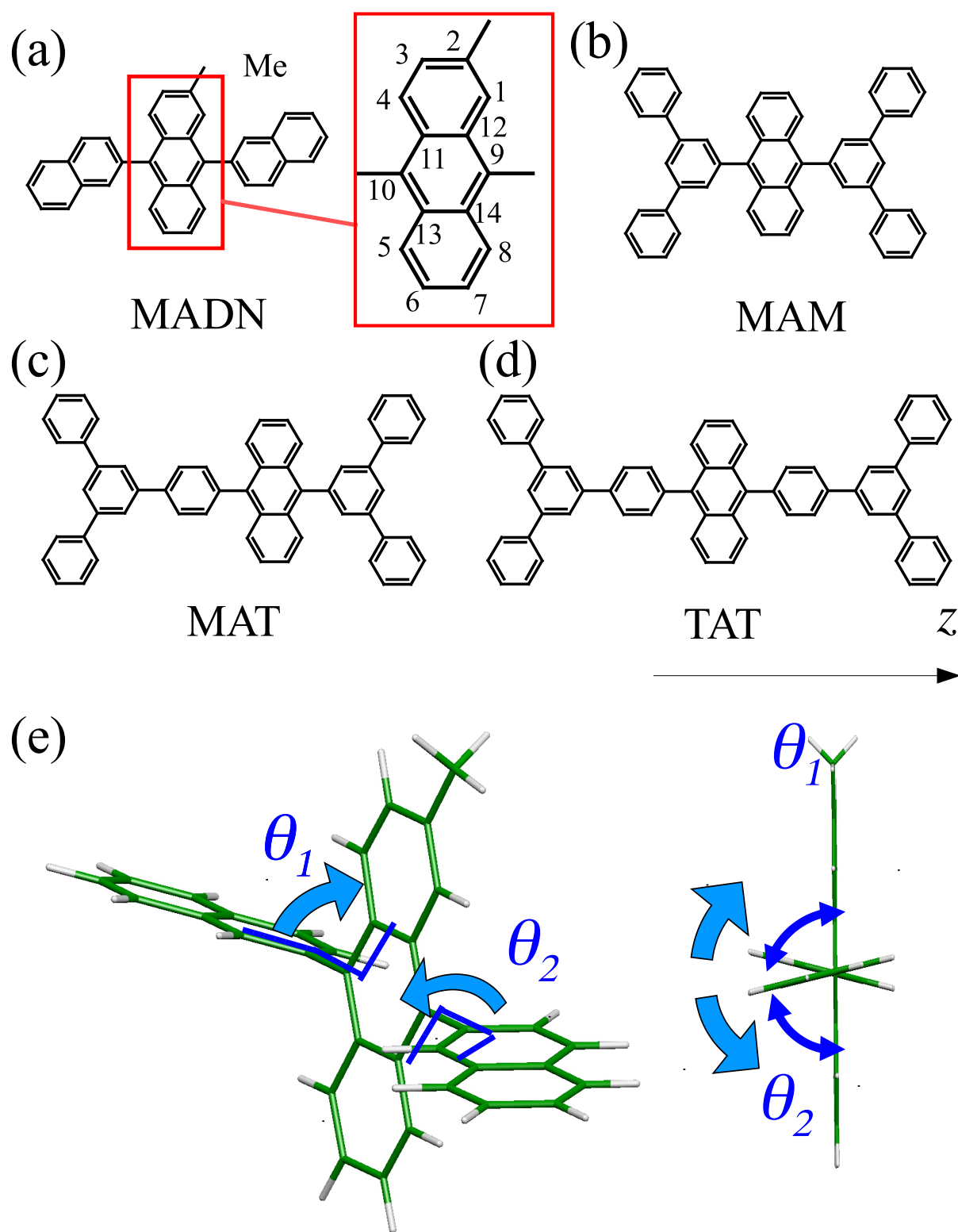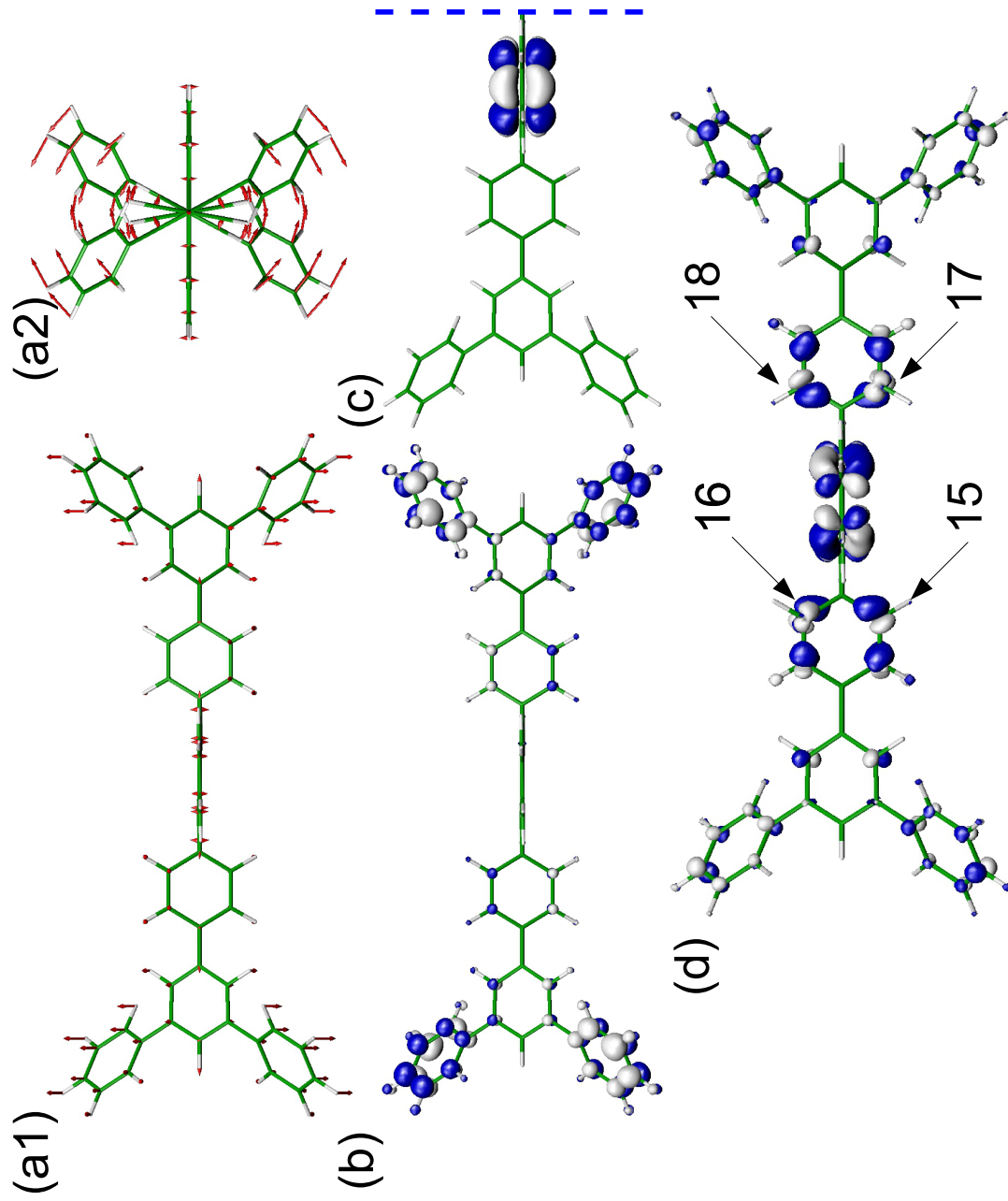
Figure 1: Uejima *et al.*
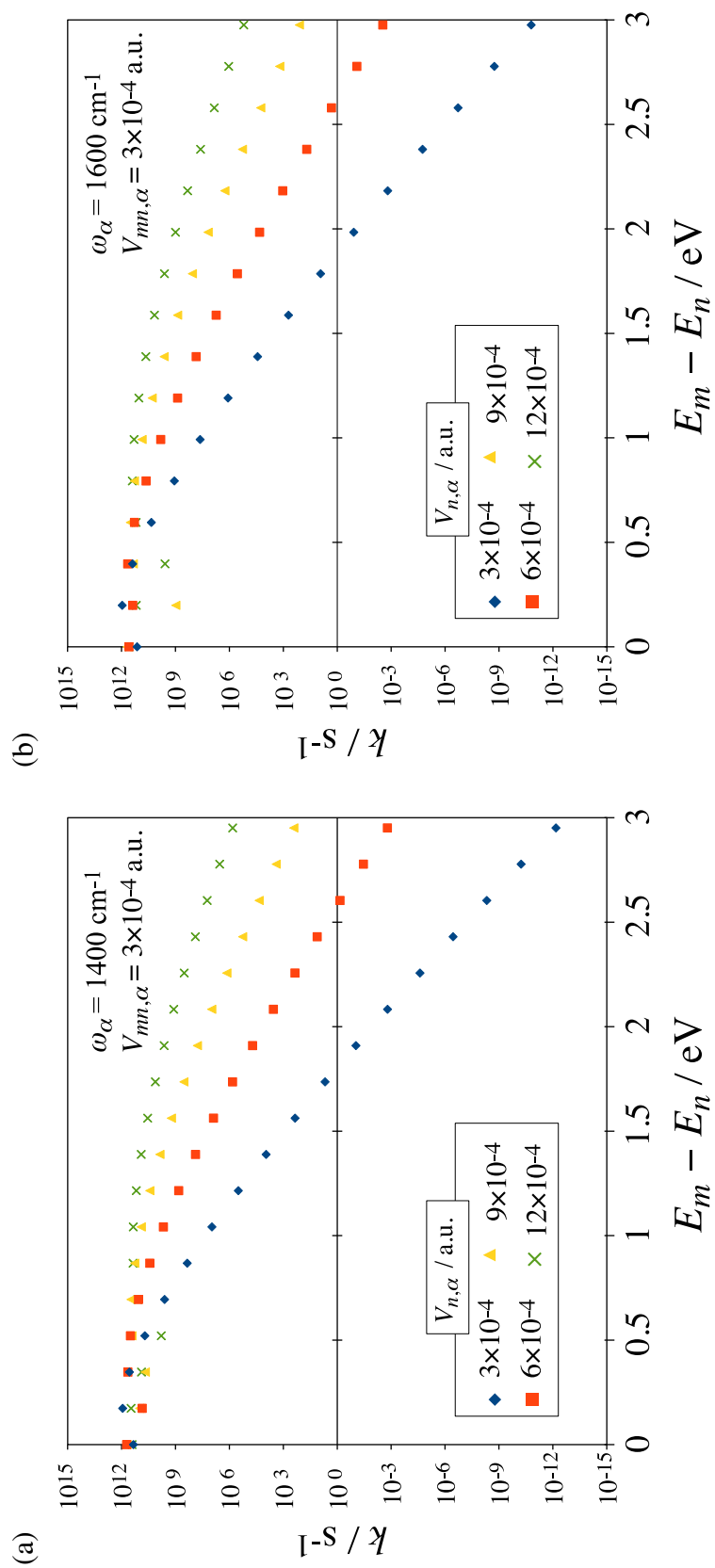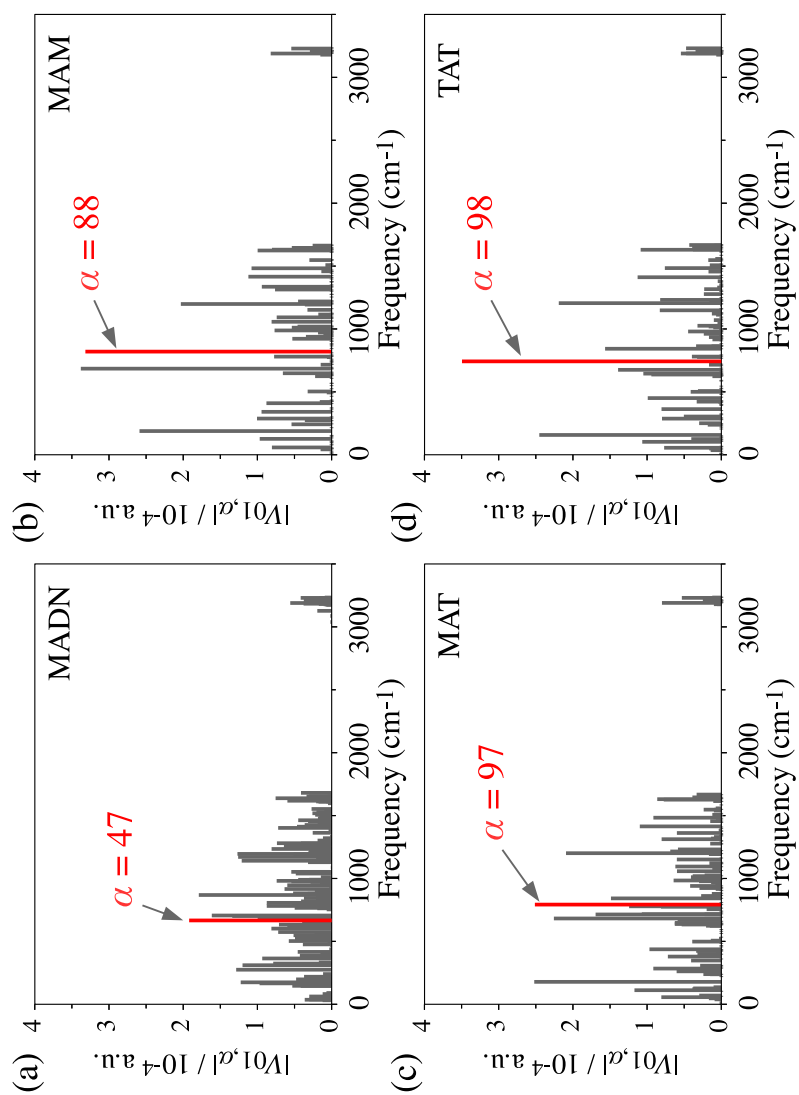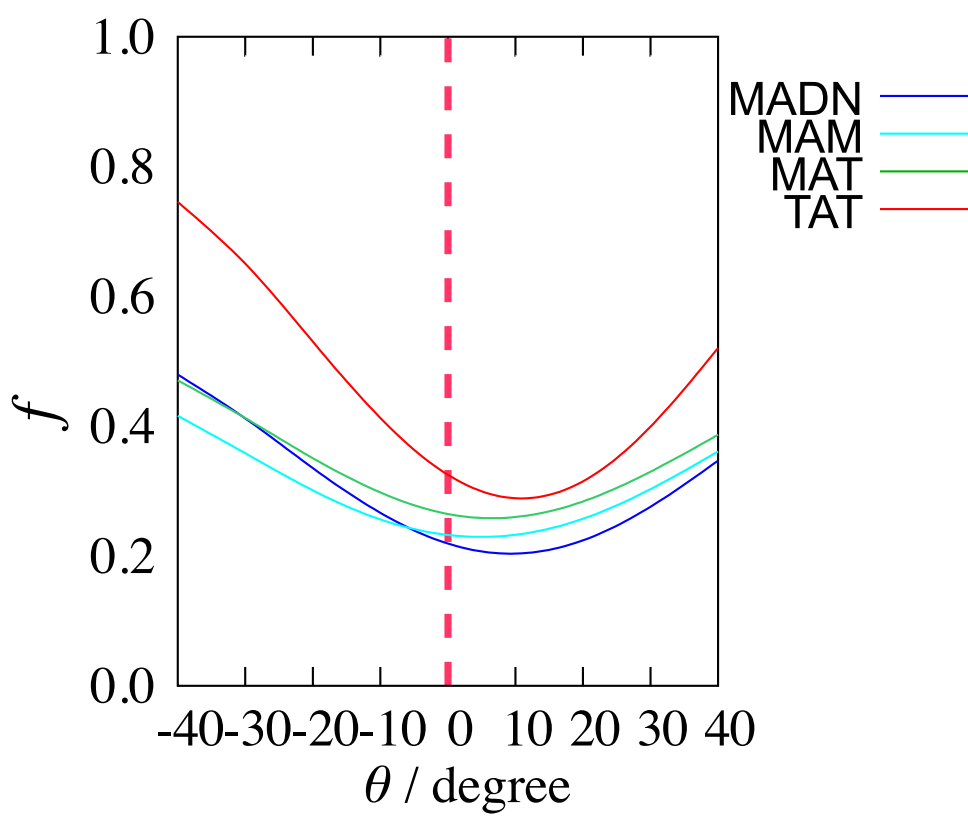
Figure 2: Uejima *et al.*
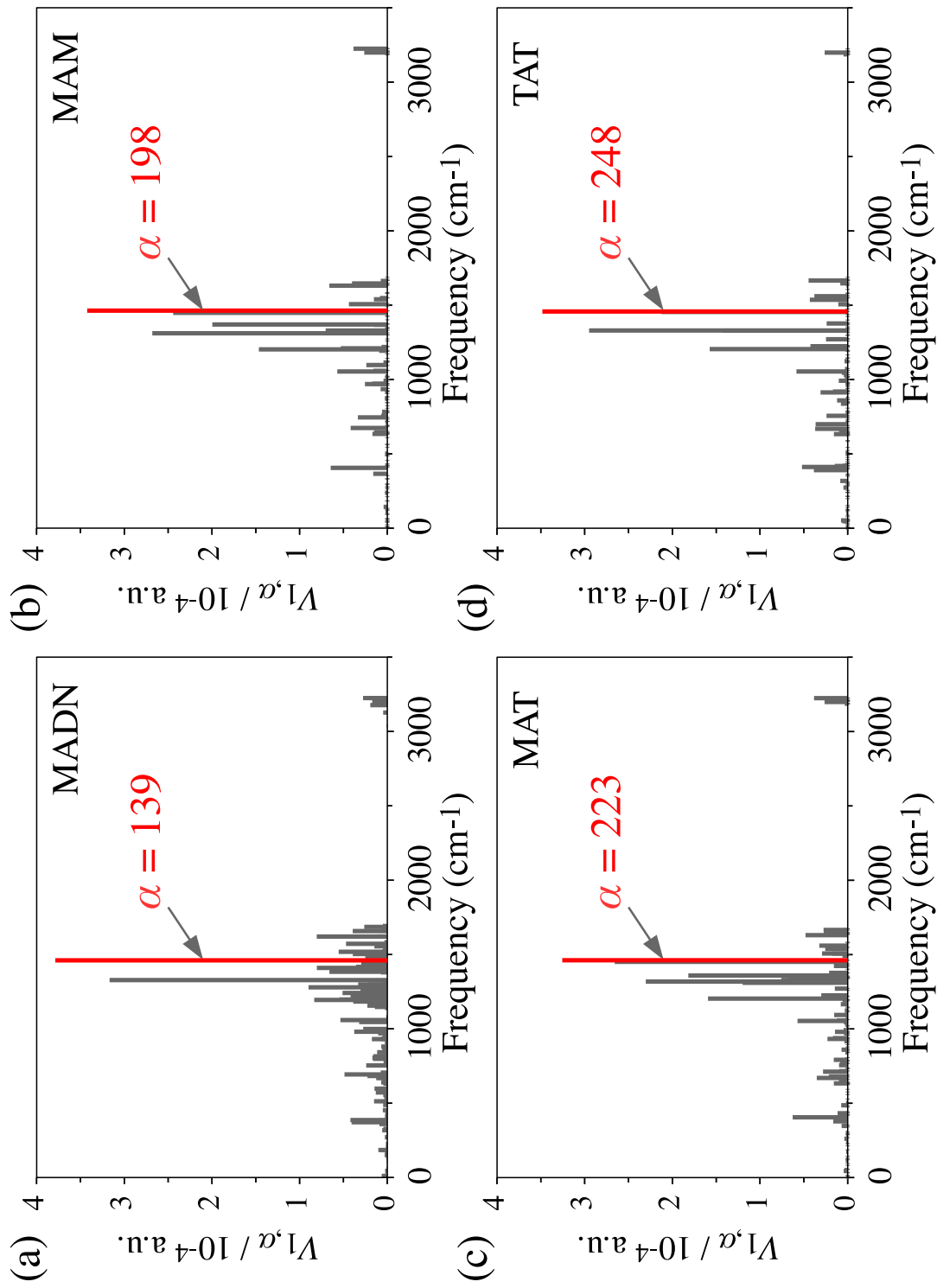
Figure 3: Uejima *et al.*
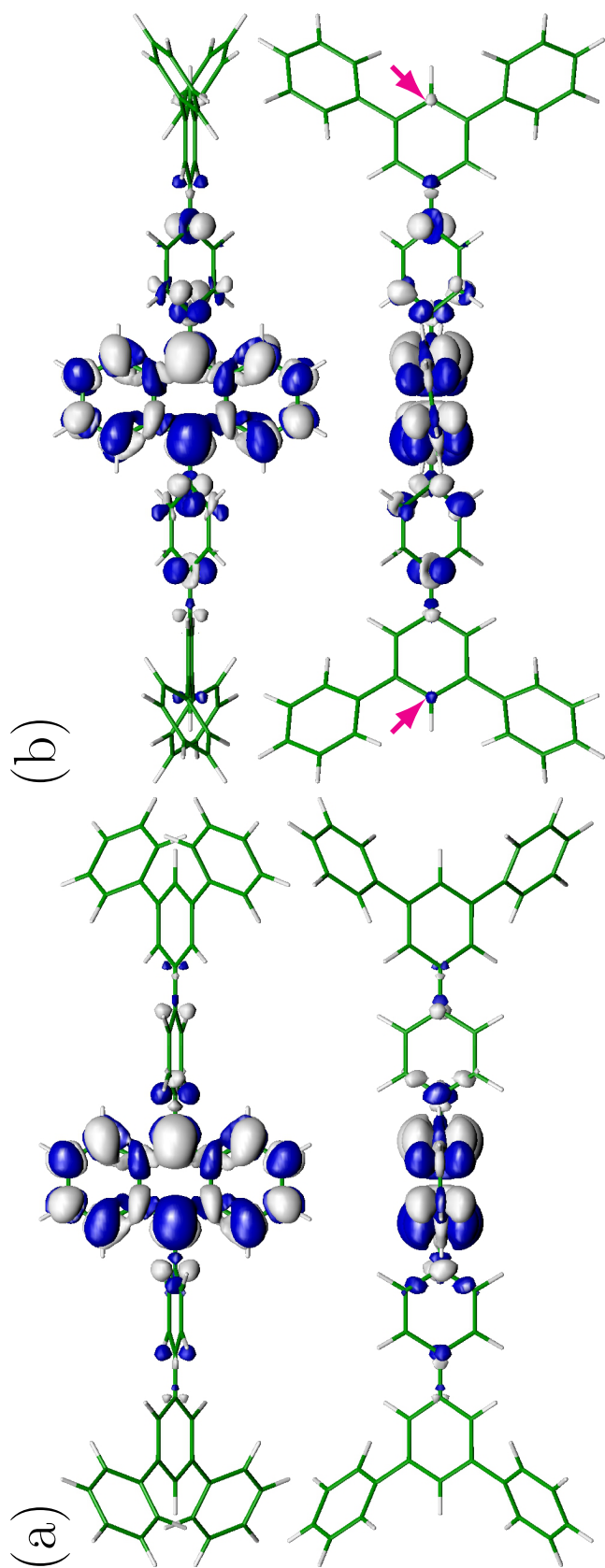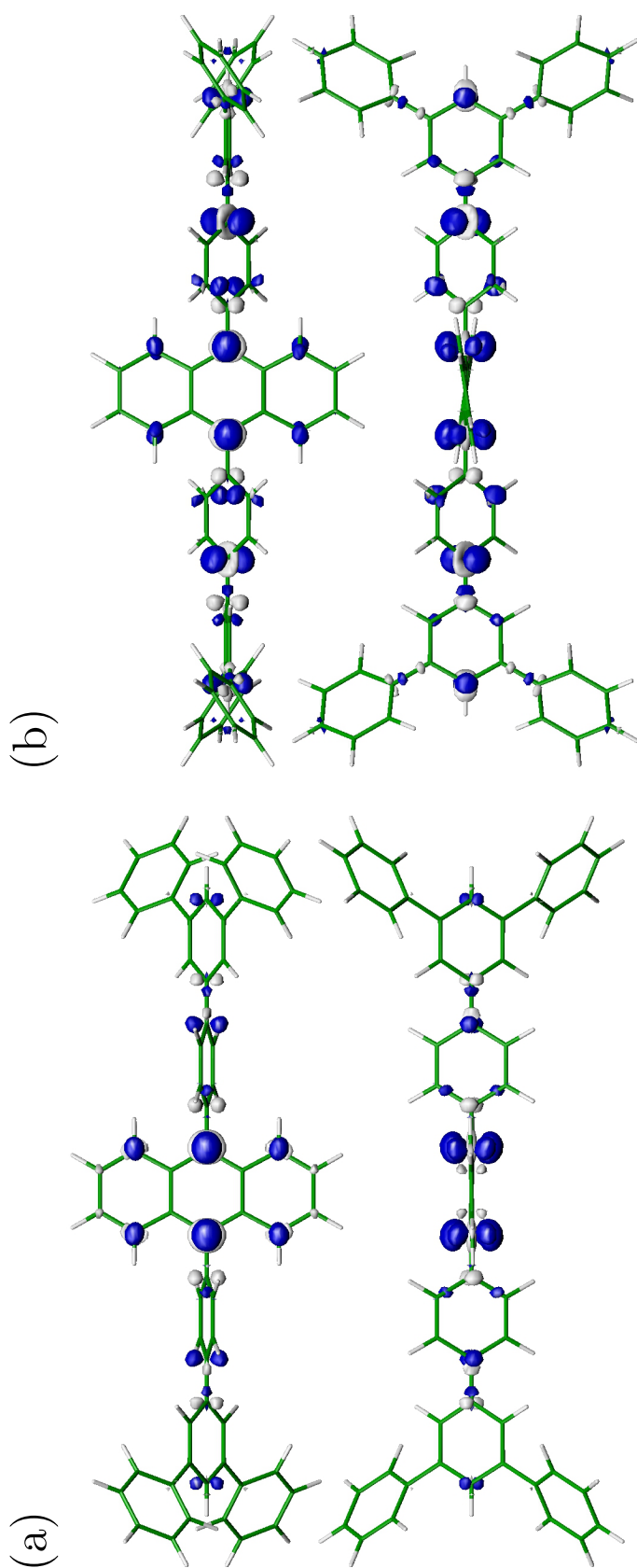
Figure 4: Uejima *et al.*

Figure 5: Uejima *et al.*

Figure 6: Uejima *et al.*

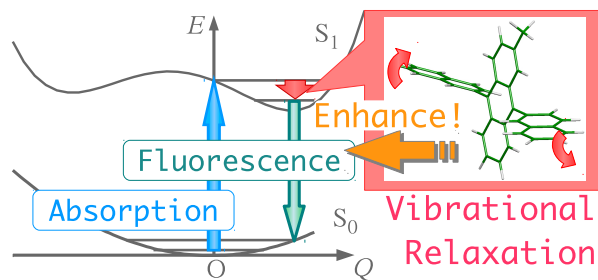Figure 7: Uejima *et al.*

Figure 8: Uejima *et al.*

Figure 9: Uejima *et al.*

Figure 10: Uejima *et al.*

(b)

(a)

Figure 11: Uejima *et al.*

Graphical abstract for the Table of Contents pages

Text: Diagonal vibronic couplings in the Franck–Condon S_1 state cause torsional distortion, which gives rise to enhancement of fluorescence with large transition dipole moment.